LETTERS

A topological Dirac insulator in a quantum spin Hall phase

D. Hsieh[1], D. Qian[1], L. Wray[1], Y. Xia[1], Y. S. Hor[2], R. J. Cava[2] & M. Z. Hasan[1,3]

When electrons are subject to a large external magnetic field, the conventional charge quantum Hall effect[1,2] dictates that an electronic excitation gap is generated in the sample bulk, but metallic conduction is permitted at the boundary. Recent theoretical models suggest that certain bulk insulators with large spin–orbit interactions may also naturally support conducting topological boundary states in the quantum limit[3–5], which opens up the possibility for studying unusual quantum Hall-like phenomena in zero external magnetic fields[6]. Bulk $Bi_{1-x}Sb_x$ single crystals are predicted to be prime candidates[7,8] for one such unusual Hall phase of matter known as the topological insulator[9–11]. The hallmark of a topological insulator is the existence of metallic surface states that are higher-dimensional analogues of the edge states that characterize a quantum spin Hall insulator[3–13]. In addition to its interesting boundary states, the bulk of $Bi_{1-x}Sb_x$ is predicted to exhibit three-dimensional Dirac particles[14–17], another topic of heightened current interest following the new findings in two-dimensional graphene[18–20] and charge quantum Hall fractionalization observed in pure bismuth[21]. However, despite numerous transport and magnetic measurements on the $Bi_{1-x}Sb_x$ family since the 1960s[17], no direct evidence of either topological Hall states or bulk Dirac particles has been found. Here, using incident-photon-energy-modulated angle-resolved photoemission spectroscopy (IPEM-ARPES), we report the direct observation of massive Dirac particles in the bulk of $Bi_{0.9}Sb_{0.1}$, locate the Kramers points at the sample's boundary and provide a comprehensive mapping of the Dirac insulator's gapless surface electron bands. These findings taken together suggest that the observed surface state on the boundary of the bulk insulator is a realization of the 'topological metal'[9–11]. They also suggest that this material has potential application in developing next-generation quantum computing devices that may incorporate 'light-like' bulk carriers and spin-textured surface currents.

Bismuth is a semimetal with strong spin–orbit interactions. Its band structure is believed to feature an indirect negative gap between the valence band maximum at the T-point of the bulk Brillouin zone and the conduction band minima at three equivalent L-points[17,22] (here we generally refer to these as a single point, L). The valence and conduction bands at L are derived from antisymmetric (L_a) and symmetric (L_s) p-type orbitals, respectively, and the effective low-energy hamiltonian at this point is described by the (3+1)-dimensional relativistic Dirac equation[14–16]. The resulting dispersion relation, $E(\mathbf{k}) = \pm\sqrt{(\mathbf{v}\cdot\mathbf{k})^2 + \Delta^2} \approx \mathbf{v}\cdot\mathbf{k}$, is highly linear owing to the combination of an unusually large band velocity $\mathbf{v}$ and a small gap Δ (such that $|\Delta/|\mathbf{v}|| \approx 5 \times 10^{-3}$ Å^{-1}) and has been used to explain various peculiar properties of bismuth[14–16]. Substituting bismuth with antimony is believed to change the critical energies of the band structure as follows (see Fig. 1). At an Sb concentration of $x \approx 4\%$, the gap Δ between L_a and L_s closes and a massless, three-dimensional (3D) Dirac point is realized. As x is further increased this gap re-opens with inverted symmetry ordering, which leads to a change in sign of Δ at each of the three equivalent L-points in the Brillouin zone. For concentrations greater than $x \approx 7\%$ there is no overlap between the valence band at T and the conduction band at L, and the material becomes an inverted-band insulator. Once the band at T drops below the valence band at L, at $x \approx 8\%$, the system evolves into a direct-gap insulator whose low-energy physics is dominated by the spin–orbit-coupled Dirac particles at L[7,17].

Recently, semiconductors with inverted bandgaps have been proposed to manifest the two-dimensional (2D) quantum spin Hall phase, which is predicted to be characterized by the presence of metallic one-dimensional edge states[3–5,12]. Although a band-inversion mechanism and edge states have been invoked to interpret the transport results in 2D mercury telluride semiconductor quantum wells[13], no one-dimensional edge states are directly imaged, so their topological character is yet to be uniquely determined. Recent theoretical treatments[7,8] have focused on the strongly spin–orbit-coupled, band-inverted $Bi_{1-x}Sb_x$ series as a possible 3D bulk realization of the quantum spin Hall phase in which the one-dimensional edge states are expected to take the form of 2D surface states[7–9] that may be directly imaged and spectroscopically studied, making it feasible to identify their topological order parameter character.

High-momentum-resolution angle-resolved photoemission spectroscopy performed with varying incident photon energy (IPEM-ARPES) allows for the measurement of electronic band dispersion along various momentum space ($\mathbf{k}$-space) trajectories in the 3D bulk Brillouin zone. ARPES spectra taken along two orthogonal cuts through the L-point of the bulk Brillouin zone of $Bi_{0.9}Sb_{0.1}$ are shown in Fig. 1a, c. A Λ-shaped dispersion whose tip lies less than 50 meV below the Fermi energy E_F can be seen along both directions. Additional features originating from surface states that do not disperse with incident photon energy are also seen. Owing to the finite intensity between the bulk and surface states, the exact binding energy E_B where the tip of the Λ-shaped dispersion lies is unresolved. The linearity of the bulk Λ-shaped bands is observed by locating the peak positions at higher E_B in the momentum distribution curves and the energy at which these peaks merge is obtained by extrapolating linear fits to the momentum distribution curves. Therefore, 50 meV represents a lower bound on the energy gap Δ between L_a and L_s. The magnitudes of the extracted band velocities along the k_x and k_y directions are $7.9 \pm 0.5 \times 10^4$ m s^{-1} and $10.0 \pm 0.5 \times 10^5$ m s^{-1}, respectively, which are similar to the tight binding values of 7.6×10^4 m s^{-1} and 9.1×10^5 m s^{-1} calculated for the L_a band of bismuth[22]. Our data are consistent with the extremely small effective mass of $0.002m_e$ (where m_e is the electron mass) observed in magneto-reflection measurements on samples with $x = 11\%$ (ref. 23). The Dirac point in

[1]Joseph Henry Laboratories of Physics, Department of Physics, [2]Department of Chemistry, [3]Princeton Center for Complex Materials, Princeton Institute for the Science and Technology of Materials, Princeton University, Princeton, New Jersey 08544, USA.

graphene, coincidentally, has a band velocity ($|\mathbf{v}_F| \approx 10^6\,\mathrm{m\,s^{-1}}$)[18] comparable to what we observe for $Bi_{0.9}Sb_{0.1}$, but its spin–orbit coupling is several orders of magnitude weaker, and the only known method of inducing a gap in the Dirac spectrum of graphene is by coupling to an external chemical substrate[20]. The $Bi_{1-x}Sb_x$ series thus provides a rare opportunity to study relativistic Dirac hamiltonian physics in a 3D condensed matter system where the intrinsic (rest) mass gap can easily be tuned.

Studying the band dispersion perpendicular to the sample surface provides a way to differentiate bulk states from surface states in a 3D material. To visualize the near-E_F dispersion along the 3D L–X cut (X is a point that is displaced from L by a k_z-distance of $3\pi/c$, where c is the lattice constant), in Fig. 2a we plot energy distribution curves (EDCs) taken such that electrons at E_F have fixed in-plane momentum $(k_x, k_y) = (L_x, L_y) = (0.8\,\text{Å}^{-1}, 0.0\,\text{Å}^{-1})$, as a function of photon energy $h\nu$. There are three prominent features in the EDCs: a non-dispersing, k_z-independent peak centred just below E_F, at about −0.02 eV; a broad, non-dispersing hump centred near −0.3 eV; and a strongly dispersing hump that coincides with the latter near $h\nu = 29$ eV. To understand which bands these features originate from, we show ARPES intensity maps along an in-plane cut $\bar{\Gamma}\bar{M}\bar{\Gamma}$ (parallel to the k_y-direction) taken using $h\nu$ values of 22 eV, 29 eV and 35 eV, which correspond to approximate k_z values of $L_z - 0.3\,\text{Å}^{-1}$, L_z, and $L_z + 0.3\,\text{Å}^{-1}$, respectively (Fig. 2b). At $h\nu = 29$ eV, the low-energy ARPES spectral weight reveals a clear Λ-shaped band close to E_F. As the photon energy is either increased or decreased from 29 eV, this intensity shifts to higher binding energies as the spectral weight evolves from the Λ-shaped band into a 'U'-shaped band. Therefore, the dispersive peak in Fig. 2a comes from the bulk valence band, and for $h\nu = 29$ eV the high-symmetry point L = (0.8, 0, 2.9) appears in the third bulk Brillouin zone. In the maps of Fig. 2b with respective $h\nu$ values of 22 eV and 35 eV, overall weak features near E_F that vary in intensity remain even as the bulk valence band moves far below E_F. The survival of these weak features over a large photon energy range (17–55 eV) supports their surface origin. The non-dispersing feature centred near −0.3 eV in Fig. 2a comes from the

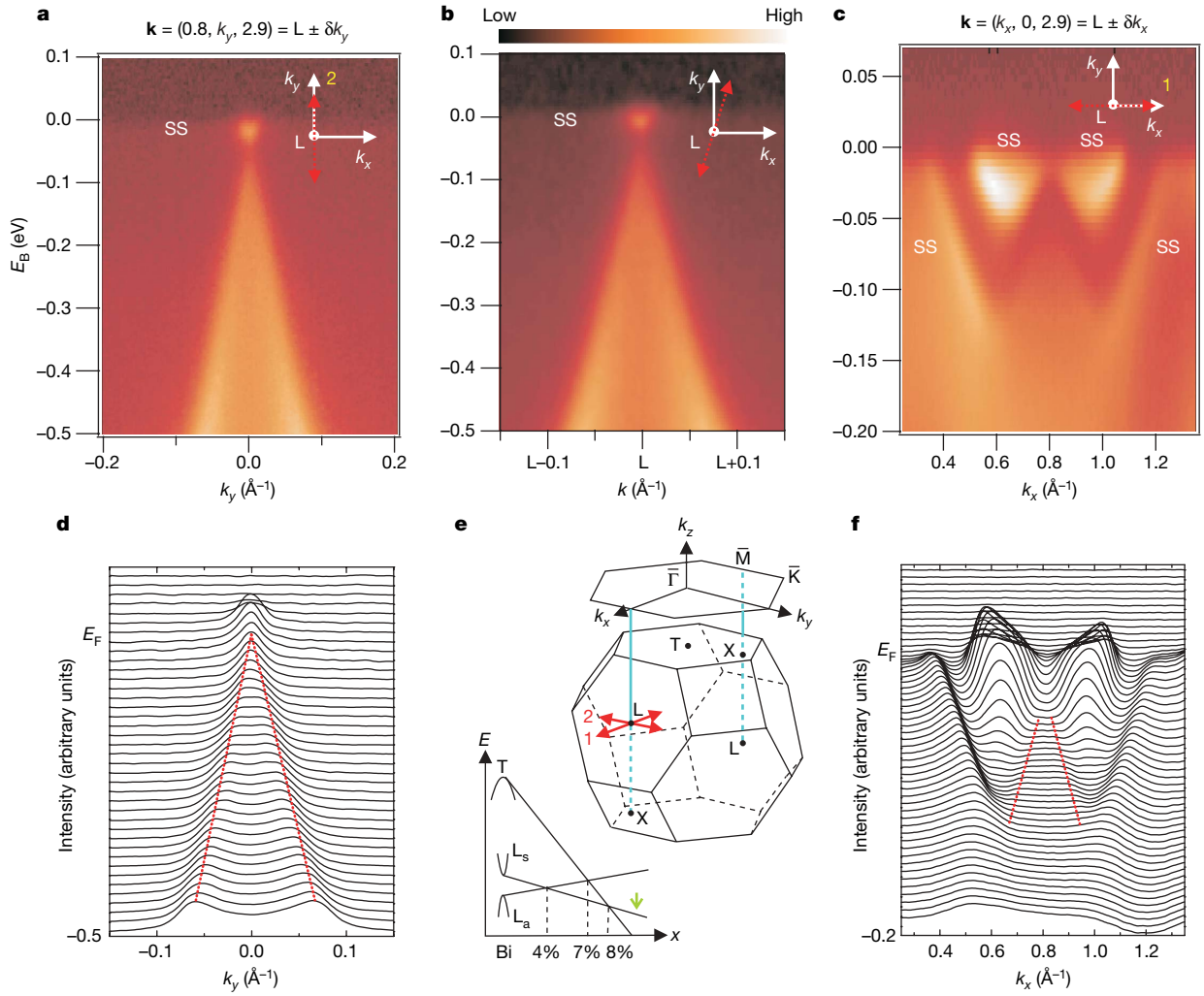

Figure 1 | Dirac-like dispersion near the L-point in the bulk Brillouin zone. Selected ARPES intensity maps of $Bi_{0.9}Sb_{0.1}$ are shown along three **k**-space cuts through the L-point of the bulk 3D Brillouin zone. The presented data are taken in the third Brillouin zone with $L_z = 2.9\,\text{Å}^{-1}$ with a photon energy of 29 eV. The cuts are along the k_y-direction (**a**); a direction rotated by approximately 10° from the k_y-direction (**b**); and the k_x-direction (**c**). Here, δ symbolizes a change along a particular **k**-direction. Each cut shows a Λ-shaped bulk band whose tip lies below the Fermi level, signalling a bulk gap. The surface states are denoted SS and are all identified in Fig. 2 (for further identification via theoretical calculations, see Supplementary Information). **d**, Momentum distribution curves corresponding to the intensity map in **a**. **f**, A log-scale plot of the momentum distribution curves corresponding to the intensity map in **c**. The red lines are guides to the eye for the bulk features in the momentum distribution curves. **e**, Schematic of the bulk 3D Brillouin zone of $Bi_{1-x}Sb_x$ and the 2D Brillouin zone of the projected (111) surface. The high-symmetry points $\bar{\Gamma}$, $\bar{M}$ and $\bar{K}$ of the surface Brillouin zone are labelled. The schematic evolution of bulk band energies as a function of x is shown. The L-band inversion transition occurs at $x \approx 0.04$, where a 3D gapless Dirac point is realized, and the composition we study here (for which $x = 0.1$) is indicated by the green arrow. A more detailed phase diagram based on our experiments is shown in Fig. 3c.

higher-binding-energy (valence band) part of the full spectrum of surface states, and the weak non-dispersing peak at −0.02 eV reflects the low-energy part of the surface states that cross E_F away from the point $\bar{M}$ and forms the surface Fermi surface (Fig. 2c).

Having established the existence of an energy gap in the bulk state of $Bi_{0.9}Sb_{0.1}$ (Figs 1 and 2) and observed linearly dispersive bulk bands uniquely consistent with strong spin–orbit coupling model calculations[14–16,22] (see Supplementary Information for full comparison with the theoretical calculation), we now discuss the topological character of its surface states, which we found to be gapless (Fig. 2c). In general, the states at the surface of spin–orbit-coupled compounds are allowed to be spin-split owing to the loss of space inversion symmetry ($E(k,\uparrow) = E(-k,\uparrow)$). However, as required by Kramers' theorem, this splitting must go to zero at the four time-reversal-invariant momenta in the 2D surface Brillouin zone. As discussed in refs 7 and 9, along a path connecting two time-reversal-invariant momenta in the same Brillouin zone, the Fermi energy inside the bulk gap will intersect these singly degenerate surface states either an even or an odd number of times. When there are an even number of surface state crossings, the surface states are topologically trivial because weak disorder (as may arise through alloying) or correlations can remove pairs of such crossings by pushing the surface bands entirely above or below E_F. When there are an odd number of crossings, however, at least one surface state must remain gapless, which makes it non-trivial[7–9]. The existence of such topologically non-trivial surface states can be theoretically predicted on the basis of the bulk band structure only, using the Z_2-invariant that is related to the quantum Hall Chern number[24]. Materials with band structures with $Z_2 = +1$ are ordinary Bloch band insulators that are topologically equivalent to the filled-shell atomic insulator, and are predicted to exhibit an even number (including zero) of surface state crossings. Materials with bulk band structures with $Z_2 = -1$, on the other hand, which are expected to exist in rare systems with strong spin–orbit coupling acting as an internal quantizing magnetic field

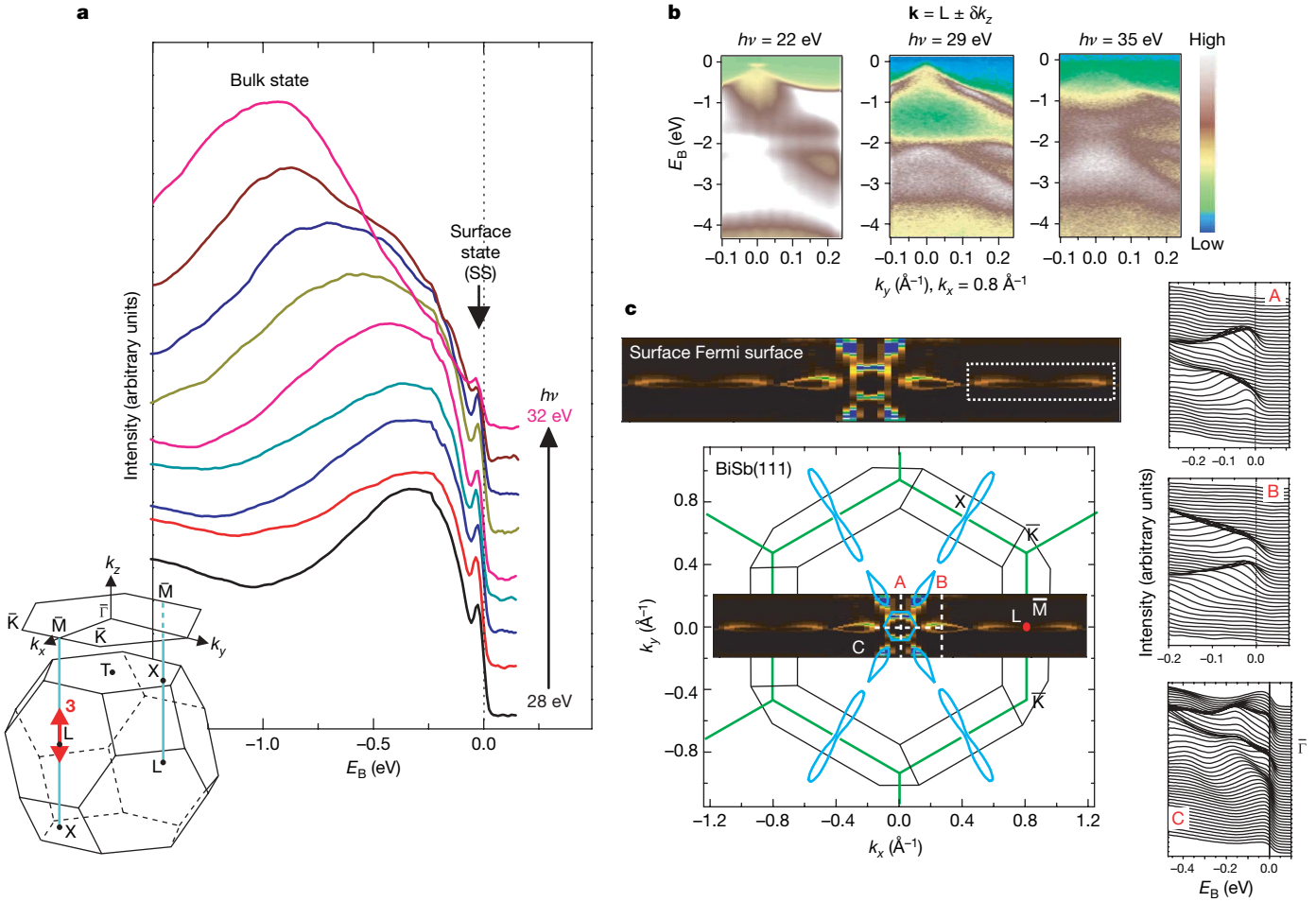

Figure 2 | Dispersion along the cut in the k_z-direction. Surface states are experimentally identified by studying their out-of-plane momentum dispersion through the systematic variation of incident photon energy. **a**, EDCs of $Bi_{0.9}Sb_{0.1}$ with electrons at the Fermi level (E_F) maintained at a fixed in-plane momentum of ($k_x = 0.8$ Å^{-1}, $k_y = 0.0$ Å^{-1}) are obtained as a function of incident photon energy to identify states that exhibit no dispersion perpendicular to the (111) plane along the direction shown by the double-headed arrow labelled '3' in the inset (see Methods for the detailed procedure). Selected EDC data sets with photon energies ranging from 28 eV to 32 eV in steps of 0.5 eV are shown for clarity. The non-energy-dispersive (k_z-independent) peaks near E_F are the surface states. **b**, ARPES intensity maps along cuts parallel to the k_y-direction taken with electrons at E_F fixed at $k_x = 0.8$ Å^{-1} with respective photon energies of $h\nu = 22$ eV, $h\nu = 29$ eV and $h\nu = 35$ eV (for a conversion map from photon energy to k_z, see Supplementary Information). The faint Λ-shaped band at $h\nu = 22$ eV and $h\nu = 35$ eV show some overlap with the bulk valence band at L ($h\nu = 29$ eV), suggesting that it is a resonant surface state degenerate with the bulk state in some limited range of momenta near E_F. The flat band of intensity centred about −2 eV in the $h\nu = 22$ eV scan originates from Bi 5*d* core-level emission from second-order light. **c**, Projection of the bulk Brillouin zone (black lines) onto the (111) surface Brillouin zone (green lines). The overlay (enlarged in inset) shows the high-resolution Fermi surface of the metallic surface state mode, which was obtained by integrating the ARPES intensity (taken with $h\nu = 20$ eV) from −15 meV to 10 meV with respect to E_F. The six teardrop-shaped lobes of the Fermi surface close to $\bar{\Gamma}$ (the centre of the Brillouin zone) show some intensity variation between them that is due to the relative orientations between the axes of the lobes and the axis of the detector slit. The six-fold symmetry was however confirmed by rotating the sample in the k_x–k_y plane. EDCs corresponding to the cuts A, B and C are also shown; these confirm the gapless character of the surface states in bulk insulating $Bi_{0.9}Sb_{0.1}$.

on the electron system[6] and inverted bands at an odd number of high-symmetry points in their bulk 3D Brillouin zones, are predicted to exhibit an odd number of surface state crossings, precluding their adiabatic continuation to the atomic insulator[3,7–13]. Such 'topological metals'[9–11] cannot be realized in a purely 2D electron gas system.

In our experimental case, namely the (111) surface of $Bi_{0.9}Sb_{0.1}$, the four time-reversal-invariant momenta are located at $\bar{\Gamma}$ and three $\bar{M}$-points that are rotated by 60° relative to one another. Owing to the three-fold crystal symmetry (A7 bulk structure) and the observed mirror symmetry of the surface Fermi surface across $k_x = 0$ (Fig. 2), these three $\bar{M}$-points are equivalent (and we henceforth refer to them as a single point, $\bar{M}$). The mirror symmetry ($E(k_y) = E(-k_y)$) is also expected, from time-reversal invariance exhibited by the system. The complete details of the surface state dispersion observed in our experiments along a path connecting $\bar{\Gamma}$ and $\bar{M}$ are shown in Fig. 3a; finding this information is made possible by our experimental separation of surface states from bulk states. As for bismuth, two surface bands emerge from the bulk band continuum near $\bar{\Gamma}$ to form a central electron pocket and an adjacent hole lobe[25–27]. It has been established that these two bands result from the spin-splitting of a surface state and are thus singly degenerate[27,28].

On the other hand, the surface band that crosses E_F at $-k_x \approx 0.5$ Å^{-1}, and forms the narrow electron pocket around $\bar{M}$, is clearly doubly degenerate, as far as we can determine within our experimental resolution. This is indicated by its splitting below E_F between $-k_x \approx 0.55$ Å^{-1} and $\bar{M}$, as well as the fact that this splitting goes to zero at $\bar{M}$ in accordance with Kramers' theorem. In semimetallic single-crystal bismuth, only a single surface band is observed to form the electron pocket around $\bar{M}$ (refs 29 and 30). Moreover, this surface state overlaps, and hence becomes degenerate with, the bulk conduction band at L (L projects to the surface point $\bar{M}$) owing to the semimetallic character of bismuth (Fig. 3b). In $Bi_{0.9}Sb_{0.1}$, on the other hand, the states near $\bar{M}$ fall completely inside the bulk energy gap, preserving their purely surface character at $\bar{M}$ (Fig. 3a). The surface

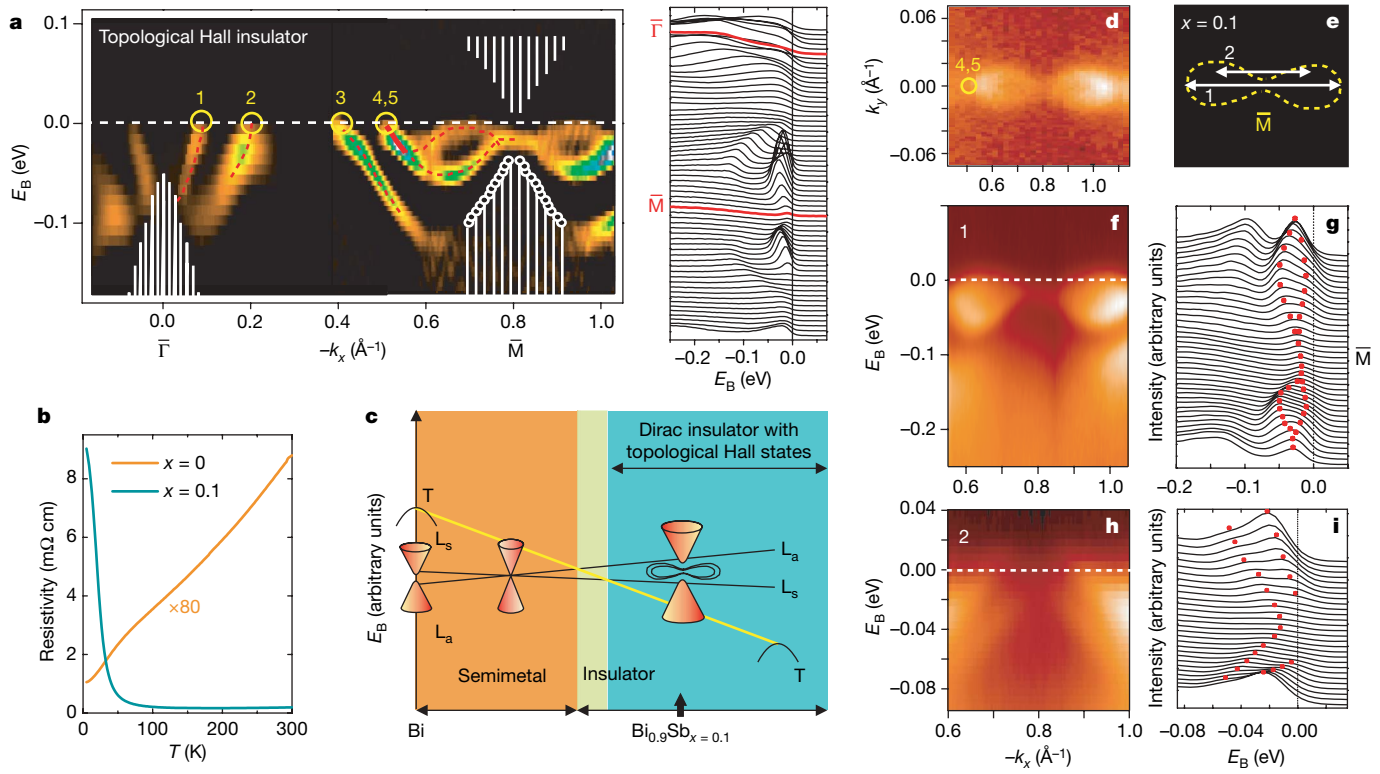

Figure 3 | The topological gapless surface states in bulk insulating $Bi_{0.9}Sb_{0.1}$. **a**, The surface-band-dispersion second-derivative image of $Bi_{0.9}Sb_{0.1}$ along $\bar{\Gamma}-\bar{M}$. The shaded white area shows the projection of the bulk bands based on ARPES data, as well as a rigid shift of the tight binding bands to sketch the unoccupied bands above the Fermi level. A non-intrinsic flat band of intensity near E_F generated by analysis of the second-derivative image was rejected to isolate the intrinsic dispersion. The Fermi crossings of the surface state are denoted by yellow circles, with the band near $-k_x \approx 0.5$ Å^{-1} counted twice owing to double degeneracy. The red lines are guides to the eye. An in-plane rotation of the sample by 60° produced the same surface state dispersion. The EDCs along $\bar{\Gamma}-\bar{M}$ are shown in the right-hand diagram. There are a total of five crossings between $\bar{\Gamma}$ and $\bar{M}$, which indicates that these surface states are topologically non-trivial. The number of surface state crossings in a material (with an odd number of Dirac points) is related to the topological Z_2 invariant (see text). **b**, The resistivity curves of Bi and $Bi_{0.9}Sb_{0.1}$ reflect the contrasting transport behaviours. The presented resistivity curve for pure bismuth has been multiplied by a factor of 80 for clarity. **c**, Schematic variation of bulk band energies of $Bi_{1-x}Sb_x$ as a function of x (based on band calculations and on refs 7 and 17). $Bi_{0.9}Sb_{0.1}$ is a direct-gap bulk Dirac point insulator well inside the inverted-band regime, and its surface forms a 'topological metal'—the 2D analogue of the one-dimensional edge states in quantum spin Hall systems. **d**, ARPES intensity integrated within ±10 meV of E_F originating solely from the surface state crossings. The image was plotted by stacking along the negative k_x-direction a series of scans taken parallel to the k_y-direction. **e**, Outline of the $Bi_{0.9}Sb_{0.1}$ surface state ARPES intensity near E_F measured in **d**. White lines show the scan directions '1' and '2'. **f**, Surface band dispersion along direction '1' taken with $h\nu = 28$ eV, and the corresponding EDCs (**g**). The surface Kramers degenerate point, critical in determining the topological Z_2 class of a band insulator, is clearly seen at $\bar{M}$, approximately 15 ± 5 meV below E_F. (We note that the scans are taken along the negative k_x-direction, away from the bulk L-point.) **h**, Surface band dispersion along direction '2' taken with $h\nu = 28$ eV, and the corresponding EDCs (**i**). This scan no longer passes through the $\bar{M}$-point, and the observation of two well-separated bands indicates the absence of Kramers degeneracy as expected, which corroborates the result in **a**.

Kramers doublet point can thus be defined in the bulk insulator (unlike in bismuth[25–30]) and is experimentally located in $Bi_{0.9}Sb_{0.1}$ samples to lie approximately 15 ± 5 meV below E_F at $\mathbf{k} = \bar{\mathbf{M}}$ (Fig. 3a). For the precise location of this Kramers point, it is important to demonstrate that our alignment is strictly along the $\bar{\Gamma}$–$\bar{\mathbf{M}}$ line. To do so, we contrast high-resolution ARPES measurements taken along the $\bar{\Gamma}$–$\bar{\mathbf{M}}$ line with those that are slightly offset from it (Fig. 3e). Figures 3f–i show that with k_y offset from the Kramers point at $\bar{\mathbf{M}}$ by less than $0.02\,\text{Å}^{-1}$, the degeneracy is lifted and only one band crosses E_F to form part of the bow-shaped electron distribution (Fig. 3d). Our finding of five surface state crossings (an odd rather than an even number) between $\bar{\Gamma}$ and $\bar{\mathbf{M}}$ (Fig. 3a), confirmed by our observation of the Kramers degenerate point at the time-reversal-invariant momentum, indicates that these gapless surface states are topologically non-trivial. This corroborates our bulk electronic structure result that $Bi_{0.9}Sb_{0.1}$ is in the insulating band-inverted ($Z_2 = -1$) regime (Fig. 3c), which contains an odd number of bulk (gapped) Dirac points, and is topologically analogous to an integer-quantum-spin Hall insulator.

Our experimental results taken collectively strongly suggest that $Bi_{0.9}Sb_{0.1}$ is quite distinct from graphene[18,19] and represents a novel state of quantum matter: a strongly spin–orbit-coupled insulator with an odd number of Dirac points and a negative Z_2 topological Hall phase. Our work points to future possibilities for further spectroscopic investigations of topological orders in quantum matter.

METHODS SUMMARY

High-resolution IPEM-ARPES data have been taken at beamlines 12.0.1 and 10.0.1 of the Advanced Light Source at the Lawrence Berkeley National Laboratory, as well as at the PGM beamline of the Synchrotron Radiation Center in Wisconsin, with photon energies ranging from 17 eV to 55 eV and energy resolutions ranging from 9 meV to 40 meV, and momentum resolution better than 1.5% of the surface Brillouin zone. Data were taken on high-quality bulk single-crystal $Bi_{1-x}Sb_x$ at a temperature of 15 K and chamber pressures less than 8×10^{-11} torr. Throughout this paper, the bulk bands presented are from those measured in the third bulk Brillouin zone, to ensure a high degree of signal-to-noise contrast, and the k_z values are estimated using the standard free-electron final-state approximation.

Full Methods and any associated references are available in the online version of the paper at www.nature.com/nature.

Received 25 November 2007; accepted 14 February 2008.

1. von Klitzing, K., Dorda, G. & Pepper, M. New method for high-accuracy determination of the fine-structure constant based on quantized Hall resistance. *Phys. Rev. Lett.* **45,** 494–497 (1980).
2. Tsui, D. C., Stormer, H. L. & Gossard, A. C. Two-dimensional magnetotransport in the extreme quantum limit. *Phys. Rev. Lett.* **48,** 1559–1562 (1982).
3. Kane, C. L. & Mele, E. J. Quantum spin Hall effect in graphene. *Phys. Rev. Lett.* **95,** 226801 (2005).
4. Bernevig, B. A. & Zhang, S.-C. Quantum spin Hall effect. *Phys. Rev. Lett.* **96,** 106802 (2006).
5. Sheng, D. N., Weng, Z. Y., Sheng, L. & Haldane, F. D. M. Quantum spin-Hall effect and topological Chern numbers. *Phys. Rev. Lett.* **97,** 036808 (2006).
6. Haldane, F. D. M. Model for a quantum Hall effect without Landau levels: Condensed-matter realization of the 'parity anomaly'. *Phys. Rev. Lett.* **61,** 2015–2018 (1988).
7. Fu, L. & Kane, C. L. Topological insulators with inversion symmetry. *Phys. Rev. B* **76,** 045302 (2007).
8. Murakami, S. Phase transition between the quantum spin Hall and insulator phases in 3D: emergence of a topological gapless phase. *New J. Phys.* **9,** 356 (2007).
9. Fu, L., Kane, C. L. & Mele, E. J. Topological insulators in three dimensions. *Phys. Rev. Lett.* **98,** 106803 (2007).
10. Moore, J. E. & Balents, L. Topological invariants of time-reversal-invariant band structures. *Phys. Rev. B* **75,** 121306(R) (2007).
11. Roy, R. Three dimensional topological invariants for time reversal invariant Hamiltonians and the three dimensional quantum spin Hall effect. ⟨http://arXiv.org/abs/cond-mat/0607531v1⟩ (2006).
12. Bernevig, B. A., Hughes, T. L. & Zhang, S.-C. Quantum spin Hall effect and topological phase transition in HgTe quantum wells. *Science* **314,** 1757–1761 (2006).
13. Konig, M. *et al.* Quantum spin Hall insulator state in HgTe quantum wells. *Science* **318,** 766–770 (2007).
14. Wolff, P. A. Matrix elements and selection rules for the two-band model of bismuth. *J. Phys. Chem. Solids* **25,** 1057–1068 (1964).
15. Fukuyama, H. & Kubo, R. Interband effects of magnetic susceptibility. II. Diamagnetism of bismuth. *J. Phys. Soc. Jpn* **28,** 570–581 (1970).
16. Buot, F. A. Weyl transformation and the magnetic susceptibility of a relativistic Dirac electron gas. *Phys. Rev. A* **8,** 1570–1581 (1973).
17. Lenoir, B. *et al.* in *Fifteenth International Conference on Thermoelectrics (Pasadena, California)* 1–13 (IEEE, New York, 1996).
18. Zhang, Y., Tan, Y.-W., Stormer, H. L. & Kim, P. Experimental observation of the quantum Hall effect and Berry's phase in graphene. *Nature* **438,** 201–204 (2005).
19. Novoselov, K. S. *et al.* Room-temperature quantum Hall effect in graphene. *Science* **315,** 1379 (2007).
20. Zhou, S. Y. *et al.* Substrate-induced bandgap opening in epitaxial graphene. *Nature Mater.* **6,** 770–775 (2007).
21. Behnia, K., Balicas, L. & Kopelevich, Y. Signatures of electron fractionalization in ultraquantum bismuth. *Science* **317,** 1729–1731 (2007).
22. Liu, Y. & Allen, E. Electronic structure of semimetals Bi and Sb. *Phys. Rev. B* **52,** 1566–1577 (1995).
23. Hebel, L. C. & Smith, G. E. Interband transitions and band structure of a BiSb alloy. *Phys. Lett.* **10,** 273–275 (1964).
24. Kane, C. L. & Mele, E. J. Z_2 topological order and the quantum spin Hall effect. *Phys. Rev. Lett.* **95,** 146802 (2005).
25. Ast, C. R. & Hochst, H. Fermi surface of Bi(111) measured by photoemission spectroscopy. *Phys. Rev. Lett.* **87,** 177602 (2001).
26. Hochst, H. & Gorovikov, S. Lack of electron-phonon coupling along two-dimensional bands in $Bi_{1-x}Sb_x$ single crystal alloys. *J. Elect. Spectrosc. Relat. Phenom.* **144,** 351–355 (2005).
27. Hofmann, P. The surfaces of bismuth: Structural and electronic properties. *Prog. Surf. Sci.* **81,** 191–245 (2006).
28. Hirahara, T. *et al.* Direct observation of spin splitting in bismuth surface states. *Phys. Rev. B* **76,** 153305 (2007).
29. Hengsberger, M. *et al.* Photoemission study of the carrier bands in Bi(111). *Eur. Phys. J. B* **17,** 603–608 (2000).
30. Ast, C. R. & Hochst, H. Electronic structure of a bismuth bilayer. *Phys. Rev. B* **67,** 113102 (2003).

Supplementary Information is linked to the online version of the paper at www.nature.com/nature.

Acknowledgements We thank P. W. Anderson, B. A. Bernevig, L. Balents, E. Demler, A. Fedorov, F. D. M. Haldane, D. A. Huse, C. L. Kane, R. B. Laughlin, J. E. Moore, N. P. Ong, A. N. Pasupathy, D. C. Tsui and S.-C. Zhang for discussions. The synchrotron experiments are supported by the DOE-BES and materials synthesis is supported by the NSF-MRSEC at Princeton Center for Complex Materials.

Author Information Reprints and permissions information is available at www.nature.com/reprints. Correspondence and requests for materials should be addressed to M.Z.H. (mzhasan@princeton.edu).

METHODS

Growth method for high-quality single crystals. The $Bi_{1-x}Sb_x$ single-crystal samples ($0 \leq x \leq 0.17$) used for ARPES experiments were each cleaved from a boule grown from a stoichiometric mixture of high-purity elements. The boule was cooled from 650 °C to 270 °C over a period of five days and was annealed for seven days at 270 °C. The samples naturally cleaved along the (111) plane, which resulted in shiny flat silver surfaces. X-ray diffraction measurements were used to check that the samples were single phase, and confirmed that the $Bi_{0.9}Sb_{0.1}$ single crystals presented in this paper have a rhombohedral A7 crystal structure (point group $R\bar{3}m$), with room-temperature (300 K) lattice parameters $a = 4.51$ Å and $c = 11.78$ Å indexed using a rhombohedral unit cell. The X-ray diffraction patterns of the cleaved crystals exhibit only the (333), (666), and (999) peaks, showing that the cleaved surface is oriented along the trigonal (111) axis. Room-temperature data were recorded on a Bruker D8 diffractometer using Cu Kα radiation ($\lambda = 1.54$ Å) and a diffracted-beam monochromator. The in-plane crystal orientation was determined by Laue X-ray diffraction. During the angle-resolved photoemission spectroscopy (ARPES) measurements a fine alignment was achieved by carefully studying the band dispersions and Fermi surface symmetry as an internal check for crystal orientation.

Transport measurements. Temperature-dependent resistivity measurements were carried out on single-crystal samples in a Quantum Design PPMS-9 instrument, using a standard four-probe technique on approximately $4 \times 1 \times 1$-mm^3, rectangular samples with the current in the basal plane, which was perpendicular to the trigonal axis. The four contacts were made by using room-temperature silver paste. The data for samples with concentrations ranging from $x = 0$ to $x = 0.17$ showed a systematic change from semimetallic to insulating-like behaviour with increasing x, in agreement with previously published works[15], which was used as a further check of the antimony concentrations. Conventional magnetic and transport measurements[7,17,31] such as these cannot separately measure the contributions of the surface and bulk states to the total signal. ARPES, on the other hand, is a momentum-selective technique[32], which allows for a separation of 2D (surface) from 3D (bulk) dispersive energy bands. This capability is especially important for $Bi_{1-x}Sb_x$ because the Dirac point lies at a single point in the 3D Brillouin zone, unlike for 2D graphene, where the Dirac points can be studied at any arbitrary perpendicular momentum along a line[33,34].

Systematic methods for separating bulk from surface electronic states. ARPES is a photon-in, electron-out technique[32]. Photoelectrons ejected from a sample by a monochromatic beam of radiation are collected by a detector capable of measuring its kinetic energy E_{kin}. By varying the detector angles, θ and φ, relative to the sample surface normal, the momentum of the photoelectrons, **K**, can also be determined (as illustrated in Supplementary Fig. 1a). By employing the commonly used free-electron final state approximation, we can fully convert from the measured kinetic energy and momentum values of the photoelectron to the binding energy, E_B, and Bloch momentum values **k** of its initial state inside the crystal, via

$$|E_B| = h\nu - W - E_{kin}$$

$$k_x = K_x = \frac{1}{\hbar}\sqrt{2m_e E_{kin}}\sin\theta$$

$$k_z = \frac{1}{\hbar}\sqrt{2m_e(E_{kin}\cos^2\theta - V_0)}$$

where we have set $\varphi = 0$, W is the work function, m_e is the electron mass and V_0 is an experimentally determined parameter, which is approximately -10 eV for bismuth[35,36]. Features in the ARPES spectra originating from bulk initial states (dispersive along the k_z-direction) were distinguished from those originating from surface initial states (non-dispersive along the k_z-direction) by studying their dependence on incident photon energy, $h\nu$, and converting this to dependence on k_z via the displayed equations. ARPES data were collected at beamlines 12.0.1 and 10.0.1 of the Advanced Light Source at the Lawrence Berkeley National Laboratory, as well as at the PGM beamline of the Synchrotron Radiation Center in Wisconsin, with incident photon energies ranging from 17 eV to 55 eV, energy resolutions ranging from 9 meV to 40 meV and momentum resolution better than 1.5% of the surface Brillouin zone, using Scienta electron analysers. The combination of high spatial resolution and high crystalline quality enabled us to probe only the highly ordered and cleanest regions of our samples. Single-crystal $Bi_{1-x}Sb_x$ samples were cleaved *in situ* at a temperature of 15 K and chamber pressures less than 8×10^{-11} torr, and high surface quality was checked throughout the measurement process by monitoring the EDC linewidths of the surface state. To measure the near-E_F dispersion of an electronic band along a direction normal to the sample surface, such as the direction from X ($2\pi/\sqrt{3}a$, 0, $8\pi/c$) to L ($2\pi/\sqrt{3}a$, 0, $11\pi/c$) shown in Fig. 2a, EDCs were taken at several incident photon energies. The kinetic energy of the photoelectron at E_F is different for each value of $h\nu$, so the angle θ was first adjusted and then held fixed for each $h\nu$ so as to keep k_x constant at $2\pi/\sqrt{3}a = 0.8$ Å^{-1} for electrons emitted near E_F. To ensure that the in-plane momentum remained constant at $\bar{\mathbf{M}}$ (the L–X line projects onto $\bar{\mathbf{M}}$) for each EDC, a complete near-E_F intensity map was generated for each photon energy to precisely locate the $\bar{\mathbf{M}}$-point (see Supplementary Fig. 1d). We note that because the bulk crystal has only threefold rotational symmetry about the k_z-axis, the reciprocal lattice does not have mirror symmetry about the $k_x = 0$ plane. Therefore, scans taken at $+\theta$ and $-\theta$ for the same photon energy probe different points in the bulk 3D Brillouin zone; this is responsible for the absence of the bulk Λ-shaped band in Fig. 3f.

31. Kopelevich, Y. *et al.* Universal magnetic-field-driven metal-insulator-metal transformations in graphite and bismuth. *Phys. Rev. B* **73,** 165128 (2006).
32. Hufner, S. *Photoelectron Spectroscopy* (Springer, Berlin, 1995).
33. Novoselov, K. S. *et al.* Two-dimensional gas of massless Dirac fermions in graphene. *Nature* **438,** 197–200 (2005).
34. Bostwick, A., Ohta, T., Seyller, T., Horn, K. & Rotenberg, E. Quasiparticle dynamics in graphene. *Nature Phys.* **3,** 36–40 (2007).
35. Jezequel, G., Thomas, J. & Pollini, I. Experimental band structure of semimetal bismuth. *Phys. Rev. B* **56,** 6620–6626 (1997).
36. Ast, C. R. & Hochst, H. High-resolution mapping of the three-dimensional band structure of Bi(111). *Phys. Rev. B* **70,** 245122 (2004).